IOP Publishing Journal of Micromechanics and Microengineering
J. Micromech. Microeng. **30** (2020) 124001 (11pp) https://doi.org/10.1088/1361-6439/abbb7d

An implantable microelectrode array for chronic *in vivo* epiretinal stimulation of the rat retina

E Yoon[1], B Koo[2], J Wong[1], S Elyahoodayan[1], J D Weiland[2], C D Lee[3], A Petrossians[3] and E Meng[1]

[1] Department of Biomedical Engineering, Viterbi School of Engineering, University of Southern California, 1042, Downey Way, DRB-140, Los Angeles, CA 90089-1111, United States of America
[2] Department of Biomedical Engineering, University of Michigan, University of Michigan College of Engineering, 2800, Plymouth Road, Building 36, Ann Arbor, MI 48105-2800, United States of America
[3] Pt Group Coatings LLC, 892 N Fair Oaks Avenue, Pasadena, CA 91103-3046, United States of America

E-mail: ellis.meng@usc.edu

Received 30 June 2020, revised 1 September 2020
Accepted for publication 24 September 2020
Published 16 October 2020

Abstract

The design, fabrication, and testing of a microelectrode array for chronic *in vivo* stimulation of the rat retina is presented. Epiretinal positioning of the array introduced design challenges associated with the surgical implantation approach into the rat ocular orbit. These anatomical and surgical challenges were overcome using microfabrication of thin-film Parylene C and platinum to create the array followed by thermal post-processing steps to achieve the required array geometry. An electroplated platinum-iridium coating was employed to increase the electrode charge storage capacity and then verified in benchtop electrochemical characterization. Preliminary *in vivo* implantations with sham devices containing no metal revealed chronic biocompatibility (up to 6 weeks) and acute trials with functional arrays illustrated device robustness against surgical trauma. This work represents the first epiretinal implant development for the rat animal model via a suitable soft neural interface device enabled through polymer MEMS micromachining.

Supplementary material for this article is available online

Keywords: epiretinal, stimulation, microelectrode array, rat, microelectrode array

(Some figures may appear in color only in the online journal)

1. Introduction

The photosensitive cells of the retina transduce light into electrical signals and enable visual perception. Access to the retina is desired to study the neural signaling involved in vision and also to introduce prostheses to restore vision to patients blinded by disease. Both can be accomplished through use of microelectrode array (MEA) neural interfaces. Because the retina is thin, spans a small area, and is mechanically delicate [1], the construction of retinal interfaces necessitates the use of soft materials and micromachining. For instance, the FDA-approved Argus II [2] retinal prosthesis features a MEA on a soft polymer substrate to provide direct electrical stimulation to the still-functional ganglion cells of the inner retina in patients with profound visual loss from retinal disease. This approach effectively bypasses the degenerated photosensitive cells in outer retinal cell layers [3].

Although some semblance of vision is provided by retinal prosthetic devices, a deeper understanding of chronic retinal stimulation on the neuroplasticity of the primary visual cortex is required to improve visual acuity and overall clinical

outcomes [4–6]. The highest visual acuity reported in Argus II clinical trials was 20/1260 [7] whereas 20/200 is legally blind in the United States and 20/20 is considered normal vision.

Animal models play an important role in vision research and may accelerate progress towards improved retinal prostheses. Clinical devices such as the Argus II were tested in canine models prior to clinical trials and were placed on the inner layer of the retina (epiretinal placement). Acute epiretinal implants in feline [8, 9] and rabbit models [10] were also reported, yet chronic implants were tested in only a handful of cases. For instance, a 120 d long study using earlier Argus I devices in canines included a limited number of animals (N = 6) [11].

The rat model is widely preferred for retinal degeneration research [12, 13]. The model is readily available at a reasonable experimental cost which facilitates meaningful study sizes. However, the size and anatomy of the rat eye impose technically challenging specifications on chronically indwelling retinal stimulation MEAs [14]. Development of rat MEAs has thus been limited to the subretinal (between the outer retinal layer and the retinal pigment epithelium) or suprachoroidal (between sclera and choroid) space in which the array can be held in place between two immuno-privileged membranes [15–17].

However, subretinal and suprachoroidal approaches suffer the marked disadvantage of indirect access to the ganglion cell layer [18]. Electrical attenuation as the device signal traverses the inner limiting membrane must be considered [19] as separation of the stimulating electrode from the retina leads to increased perceptual threshold [20]. Conversely, the main advantage of the epiretinal approach is the direct access to still-functional inner retinal layers albeit accompanied by notoriously challenging surgeries. Retinal detachment, hypotony, infection or other serious adverse events are more likely to occur in epiretinal operations due to the retina's extremely delicate nature [21]. Such challenges in surgical access have limited epiretinal studies of rat retino-cortical relationships to cases where investigators resorted to manual point-by-point epiretinal probing with needle electrodes on anaesthetized rats in acute settings [22, 23].

Given the importance of the rat model in vision research, an indwelling epiretinal MEA was developed to enable investigation of chronic epiretinal stimulation in rats. Polymer micromachining was leveraged to produce an intricately shaped MEA from thin-film Parylene C substrates and platinum (Pt) [24]. An electrodeposited platinum-iridium (PtIr) alloy coating was applied to electrode sites to facilitate stimulation efficiency [25, 26]. The nuanced design requirements, fabrication processes, and benchtop characterization are described in this work. Implementation of devices *in vivo* demonstrated device robustness against mechanical trauma from the implantation procedure and suitability for use in vision research.

2. Design

2.1. Anatomical considerations

The ocular and cranial anatomy of the rat give rise to challenging design constraints for an epiretinal interface. The rat eye orbit is significantly smaller (diameter $\approx$ 5 mm) [27] than that of other species used in retinal stimulation studies such as rabbit, guinea pig, and sheep [14]. The small orbit limits the size of the MEA and therefore the total number of microelectrodes that may be packed onto the device. Mechanical fixation of MEAs to secure them in close proximity to the retina is traditionally achieved using a retinal tack in larger species [28, 29]. However, tacking would leave a prohibitively large puncture wound relative to the size of the rat orbit. This wound would cause a decrease in intraocular pressure leading to globe deflation and loss of vision. Thus, an alternative fixation method is required in the rat model.

Additionally, the rat eye has a considerable range of motion in several axes, some not available in humans. Rats can temporarily proptose their ocular globes slightly out of the socket. They are also capable of ocular torsion (rotation around the optical axis) and cycloversion (rotation of both eyes in the same direction) [30]. Hence, flexibility or slack in the cable connecting the stimulating region to downstream electronics is required in order to minimize abrasion and irritation between the device and the delicate retina.

Lastly, the length of the device ribbon cable must match the distance from the eye socket to the skull where downstream electronics are fitted onto a headcap. These aspects as well the ease of handling during the surgical implantation procedure were factored into the overall design concept (figure 1).

The stimulation region is located in left-most portion of the concept illustration. This MEA contains two rows of four electrodes, where the top row varies in electrode diameter and bottom row has constant diameter (figure 2); the motivation for this approach is to allow determination of optimal electrode dimensions during *in vivo* experiments [31–33]. Electrodes A, B, C, and D have exposed diameters of 210, 90, 60 and 40 μm; respectively. The exposed diameters of electrodes E, F, G, and H are all 160 μm. Different stimulation region lengths were designed (2.0, 2.5, and 3.0 mm) to account for any potential variability in rat retinal size.

The stimulation region width is 780 μm and this value is a tradeoff between maximizing the number of electrodes on an array and minimizing the scleral incision size. This value was determined through preliminary surgical experiments and set to avoid drops in intraocular pressure and subsequent globe rupture for scleral incisions exceeding approximately 1 mm. Wires for the electrodes are 30 μm wide with 30 μm spacing.

The wires taper out from the stimulation region into the ribbon cable region (figure 1) in order to provide the surgeon with a wire-free region for handling. Alternatively, grasping tabs on the side of the ribbon cable region were included. The surgeon

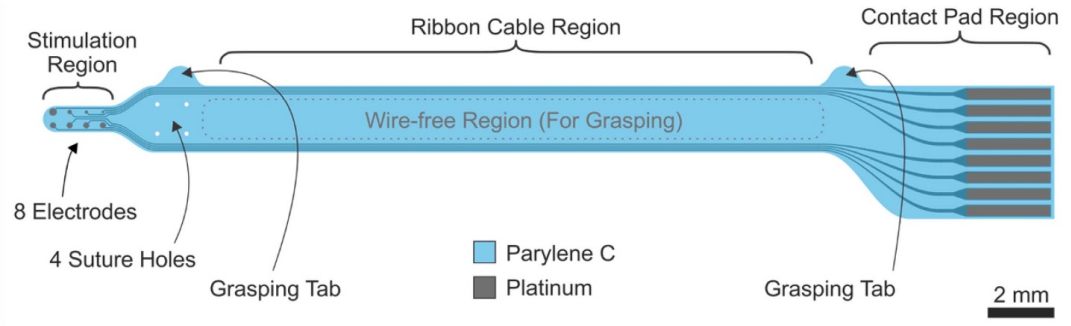

Figure 1. Design schematic of rat retinal microelectrode array illustrating three major regions and main features.

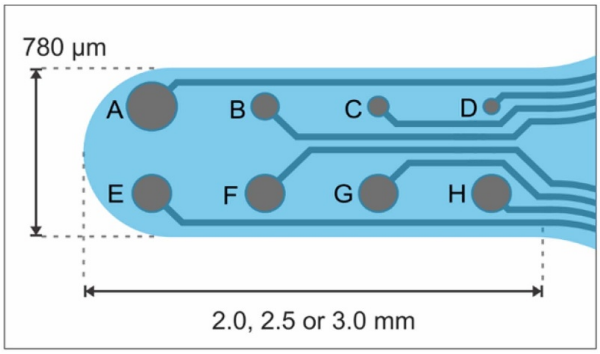

Figure 2. Magnified view of eight electrodes at the stimulation region.

can manipulate the MEA in these regions with fine and sharp tweezers without fear of damaging the wires or compromising electrical insulation. Suture holes allow device fixation onto the eye via sutures onto the sclera which provides a suitable alternative to retinal tacks. The array terminates in eight contact pads which are sized to mate with commercial connectors attached to downstream electronics.

Standard MEMS fabrication processes yield flat and planar structures whereas the retina resembles a three-dimensional hemispherical shell. Therefore, a thermoforming process was applied to arrays [34] to confer a curled shape at the tip (figure 3). This improves electrode-to-retina proximity to increase stimulation efficiency because electric field strength attenuates with distance squared [35]. The length of the stimulating region was intentionally designed to match the arc length of the upper temporal quadrant only. Although it is possible to create designs which span the entire retinal arc, preliminary surgical experiments revealed that doing so increased the rates of retinal tearing or detachment. The upper temporal quadrant also contains the highest density of rat retinal ganglion cells [36]. Additionally, shortening the arc length allowed the MEA and surgical procedure to better accommodate the large lens which occupies a larger portion of the ocular orbit compared to other species [37]. Contact with the lens may leave scratches resulting in cataract formation.

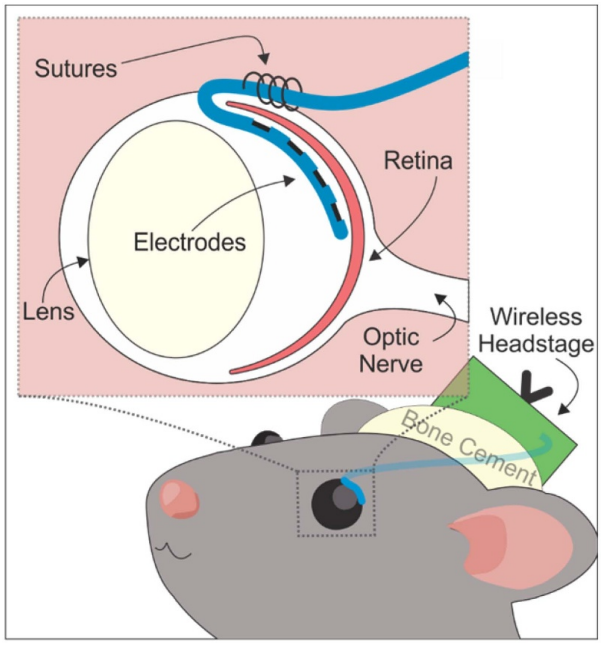

Figure 3. Shaping of the array through thermoforming allows for retinal curvature matching.

3. Materials and methods

3.1. Fabrication and packaging

The design and fabrication of the arrays were performed in a two-step process. First, sham arrays containing only Parylene C were rapidly prototyped to quickly assess surgical feasibility in several design iterations. Second, arrays with electrodes were fabricated once the final geometry was set. Parylene C, herein referred to as Parylene, was selected as the substrate material due to its biocompatibility and amenability to microfabrication techniques [24].

Shams were constructed by cutting sheets of 20 μm thick Parylene using a motorized vinyl cutter (Graphtec CE-6000, Graphtec America Inc. Irvine, CA). The sheet was obtained

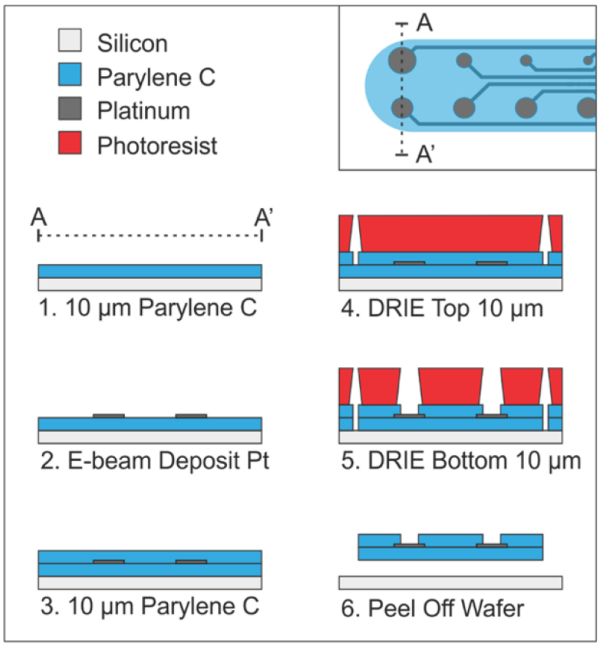

Figure 4. Microfabrication process for rat retinal stimulation array.

through two depositions of 10 μm thick Parylene with a PDS Labcoter 2010 (Specialty Coating Systems, Indianapolis, IN) via room temperature chemical vapor deposition onto a dehydrated (12 h 90 °C) 4" silicon wafer (University Wafers, South Boston, MA). The Parylene was carefully sliced and peeled off of the wafer and loaded onto the cutter.

Functional arrays were fabricated using established surface micromachining processes [18, 35] (figure 4). A single 10 μm thick layer of Parylene was deposited on a silicon carrier wafer and then AZ 5214E image reversal photoresist (Integrated Micro Materials, Argyle, TX) was spun on and patterned to define the metal wires, electrodes, and contact pads. An O_2 plasma descum (60 s, 100 W, 100 mTorr) was performed immediately prior to electron beam evaporation of 99.99% Pt (PraxAir Inc. Danbury, CT) by using a CHA Mark 40 system (CHA Industries, Fremont, CA).

In total, 200 nm of Pt was deposited, but special care was required to prevent metal cracking due to the thermal expansion coefficient mismatch between Parylene and Pt. Without breaking vacuum, the 200 nm of Pt was split into four deposition steps of 50 nm with 30-min pauses between each step. The deposition rate was 1.5 Å s^{-1}. The resting steps and a long chamber throw distance (21.5") were crucial in providing enough cooling of the substrate. Metal liftoff was performed in sequential baths of acetone, isopropanol (IPA), and deionized water each for 10 min at room temperature.

After liftoff, another O_2 descum was performed and then an additional 10 μm layer of Parylene was deposited. Next, a layer of AZ P4620 photoresist (Integrated Micro Materials, Argyle, TX) was used to define the cutout outline shape and suture holes for the arrays. The photoresist served as the protecting mask as the wafer underwent a switched chemistry process in a deep reactive ion etching (DRIE) tool that alternated between fluoropolymer deposition (C_4F_8) and oxygen plasma etching [24]. Etching with this mask proceeded until the top 10 μm of Parylene was removed, as measured by Dektak XT Profilometer (Bruker, Billerica, MA). After photoresist stripping, another AZ P4620 layer was spun on as a photoresist mask which defined the cutout outline, suture holes, and also the openings for the electrodes and contact pads. Next was another DRIE step to simultaneously expose the metal at the electrodes and contact pads while completing the cutout and suture etch down to the silicon substrate.

Deionized water drops were applied to individual devices to facilitate release by carefully peeling off the wafer with tweezers. To ensure that all residual photoresist was removed, devices were then cleaned at room temperature in sequential baths of acetone, IPA, and deionized water.

Devices were then thermoformed (200 °C, 48 h, 3 × nitrogen purged) while mounted in a custom mold (figure S1 (available online at stacks.iop.org/JMM/30/124001/mmedia)) to obtain the appropriate curled shape. A subset of devices was thermoformed flat (herein referred to as annealed) to allow for imaging with compound microscopes. Annealed arrays were coated in platinum-iridium (PtIr) via an electrodeposition method [25, 38] to lower electrochemical impedance and improve charge storage capacity.

Packaging was accomplished by zero insertion force (ZIF) connectors (Hirose Electric Co., Ltd, Tokyo, Japan) mated to the Pt contact pads. A polyethylene terephthalate (PET) backing provided the necessary thickness (~200 μm) for the ZIF to engage its closing latch. The backing was cut with a motorized cutter to match the shape of the overall contact pad region to facilitate proper insertion into the ZIF. Unlike previous ZIF packaging techniques which employed cyanoacrylate adhesive [39], this technique permitted reversible ZIF connections to allow characterization between cumulative post-fabrication processes such as thermoforming, annealing or PtIr coating. This scheme also allowed for temporary connections to benchtop electrochemical testing equipment and then to wireless headstage equipment via a custom printed circuit board (figure S2) for use in envisioned chronic animal experiments.

3.2. *Electrochemical testing*

A Gamry Reference 600 Potentiostat (Gamry Instruments, Warminster, PA, USA) was used in all electrochemical experiments. An Ag/AgCl electrode (3 M NaCl) (Basi® Inc., West Lafayette, IN) was the reference and a 1 cm long and 0.5 mm diameter Pt wire (World Precision Instruments, Sarasota, FL) was the counter. The electrolyte was either 1 × phosphate buffered saline (PBS) to mimic the vitreous humor [40] or 0.05 M H_2SO_4 (with 10 min of N_2 bubbling) for cleaning at room temperature. Potentiostatic electrochemical impedance spectroscopy (EIS) was carried out from 1 Hz to 10 MHz with a 25 mV perturbation signal and no DC bias. Cyclic voltammetry (CV) was conducted at 100 mV s^{-1} with −0.6 to 0.8 V endpoints with respect to the reference. Thirty cycles initiated and terminated at 0 V with respect to the average open circuit

potential to avoid unintentional surface conditioning. Gamry Framework Custom Scripts (Galv Repeating Pulse) applied five charge balanced, cathodic first, biphasic pulses with current densities and phase durations based on similar work [22] (30 μC cm^{-2}, 500 μs width, 100 μs gap) were applied to MEAs. Typical pulse current amplitudes in rat epiretinal studies for neuroplasticity may range from $\pm$5 to 100 with 1 Hz frequency, 100 μs gap, and 50% duty cycle [22]. The recorded voltage was averaged and normalized to open circuit potential values.

3.3. Animal surgeries

Preliminary surgeries with Parylene-only sham devices were conducted on iterative designs. Sham devices were sterilized by ethylene oxide gas. The devices were then implanted in the left eye of male Long-Evans rats (n = 2, 3–4 months, 250–350 g) to evaluate the design and surgical technique.

All procedures for sham devices were performed in accordance to a protocol approved by the Animal Care and Use committee at the University of Southern California. Rats were anesthetized by an intramuscular injection of ketamine and xylazine mixture, lasting approximately 2 h. During the surgery, the anesthetic depth was periodically monitored via 'toe-pinch' response. If a response was elicited, the animal r eceived another half dose of anesthetic.

In sham surgeries, the ribbon cable was sliced off such that only the stimulation region and suture hole section remained in order to focus on implant feasibility. A 6–0 suture was used to hook and pull away the top eyelid for better access to the eye. Surgical scissors cut 2 mm of the conjunctiva to help create an incision on the sclera. The tip of a 30-gauge needle was used to slowly rub the sclera for conjunctiva removal. Then, a 10–0 suture needle was used to pass through the suture section, hooked on the sclera near the incision, and a loose knot was made. The tab was grasped by fine tweezers to push the device through the incision at an acute angle to avoid contacting the cornea. Once inside the orbit, the device was positioned at the upper temporal quadrant and the loose knot was tightened. The animal recovered in warm bedding and returned to its holding once able to move around normally again. Animals were monitored for pain, inflammation and infection for up to 2 weeks post-surgery. From week 2 up to week 6, animals were anesthetized once a week to image with optical coherence tomography (OCT) and fundus imaging.

MEA device experiments were conducted at the University of Michigan in accordance to a protocol approved by their Institutional Animal Care and Use Committee. A Long-Evans rat was anesthetized in 3.0% isoflurane and maintained at 2.3% to eliminate toe-pinch reflex. The animal was secured on a stereotaxic frame and the head was secured with ear bars. After shaving and alternating between 70% ethanol and betadine cleansing three times, a longitudinal incision was made over the skull along the midline. The skin was parted and the fascia was removed to expose the cranial bone. A drill hole was made 2.0 mm anterior to the bregma suture with a dental drill. A stainless-steel machine screw was bored into the drill hole for the counter/reference. Silicone elastomer was applied on top of and around the machine screw to ensure electrical isolation of the counter/reference electrode.

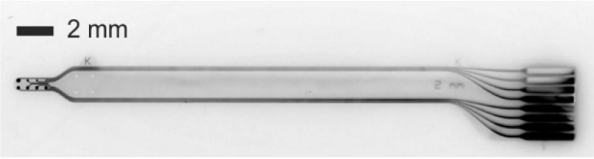

Figure 5. Fully fabricated retinal array immediately after removal from carrier wafer.

The eye was proptosed by routing a 5–0 silk suture past the temporal eyelid and pulling the eyelid towards the midline. A peritomy was performed with iris scissors on the conjunctiva 1 mm away from the limbus on the temporal edge of the eye. A blunt dissection of the conjunctiva separated it from the underlying sclera, completing the peritomy. A 20-gauge needle was introduced under the conjunctiva to create the initial hole for routing the array. The needle was removed, and a 12-gauge needle was introduced to create a tunnel for the device. The array was introduced into the needle lumen and the needle was pulled back, acting as a vehicle to transport the Parylene array into the eye. A 30-gauge needle was used to create the sclerotomy for array insertion. Implanted devices were thermoformed with bare Pt electrodes.

Care was taken to avoid the lens during needle insertion and sclerotomy expansion to avoid cataract formation. An 8–0 suture was threaded into the first suture hole in the device and the suture needle was incised in the sclera 1 mm away from the sclerotomy, directing the suture parallel to the sclerotomy. After the suture was threaded into the other suture hole, the device was lowered towards the eye, inserting the stimulation region into the sclerotomy using a second 30-gauge needle for support. The suture was then tied down to anchor and align the device.

4. Results

4.1. Fabrication

Figure 5 shows a representative device. Post-processing procedures such as thermoforming and PtIr coating were carried out and shown in figures 6 and 7. The thermoformed array has a 2.5 mm radius of curvature at the electrode region and spans the upper temporal quadrant as designed. The array then folded back in order to guide the ribbon cable towards the PCB headstage.

The other post-processing technique was electrodeposition of PtIr (figure 7). Its nanofractal surface absorbs light more effectively than bare Pt. This causes the difference in electrode coloration from the originally reflective bare Pt to the

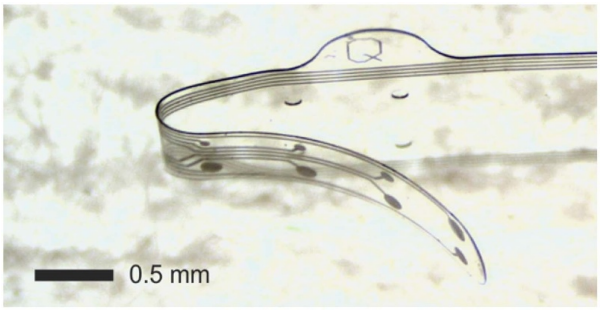

Figure 6. Thermoforming technique permits fabrication of curled array tip to match retinal curvature.

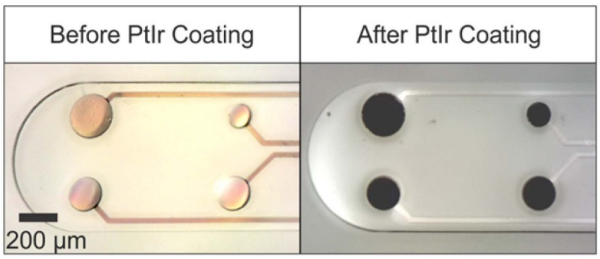

Figure 7. Magnified view of electrodes before (a) and after (b) electrodeposition of PtIr.

solid black PtIr which is limited to the electrode sites and not observed on the wires.

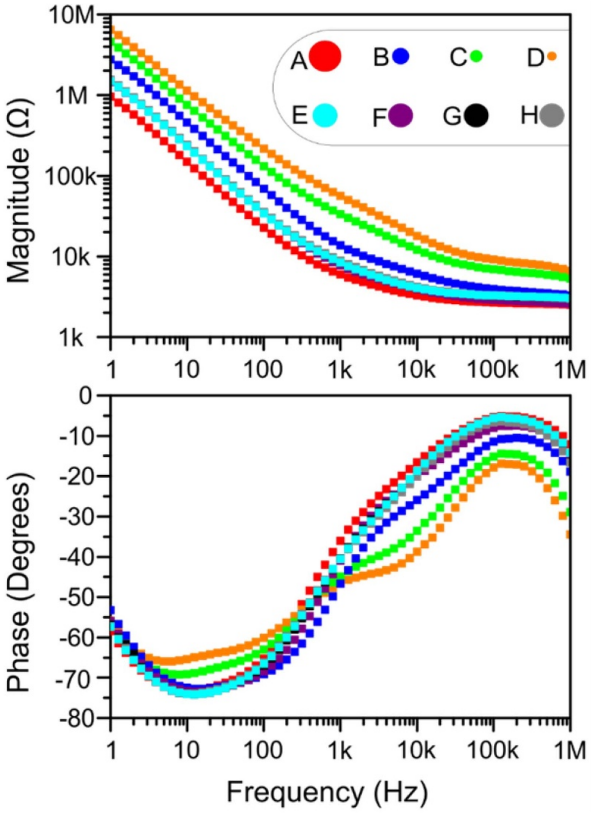

Figure 8. Impedance magnitude (a) and phase (b) of each electrode in an unannealed device (1 × phosphate buffered saline, 25 °C).

4.2. Electrochemical characterization

After fabrication, devices were packaged and underwent EIS testing. A representative plot of the impedance magnitude and phase for one unannealed array is displayed in figure 8. Note that distinct spectra can be observed for each electrode size. Since electrodes E, F, G, and H have the same 160 μm diameter, their EIS data are closely overlapped.

Electrochemical properties of the electrodes after post-processing were also investigated. EIS values from the equally sized electrodes (electrodes E, F, G, and H) were averaged and plotted for devices that had been unannealed, annealed, thermoformed, and PtIr coated (figure 9). Both two-dimensional annealing and three-dimensional thermoforming caused a shift in electrochemical impedance spectra relative to their unannealed starting point, but no significant difference existed between annealed and thermoformed devices. This suggests that thermal treatment yields electrochemically similar results regardless of device planarity.

PtIr coating was electrodeposited onto an annealed device and figure 9 shows that this caused an approximately 10 × reduction in the 1 kHz impedance magnitude. Although the geometric surface area of the electrodes remained the same,

the electroactive surface area was dramatically increased due to the coating's fractal surface roughness properties [38]. This formation of additional electrochemical reaction sites serves to lower electrochemical impedance and hence increase charge storage capacity.

The same devices at these various stages of post-processing were also characterized through CV and the average of all 30 cycles per device condition was plotted (figure 10). PtIr coated arrays exhibited the widest current range in CV plots, indicating that they possess the largest charge storage capacity. Between annealed and thermoformed cases, there was no significant difference. Characteristic peaks and valleys corresponding to hydrogen adsorption and desorption, double layer charging, and Pt-oxide redox reactions [41] were present for bare Pt in thermally treated devices (figure S3), but not readily observable in the unannealed case.

The slow sweep rates in the CV technique are known to present limitations in the context of characterizing stimulation microelectrodes [42] due to differing time scales present in rapid stimulation pulses [43]. Therefore, pulse tests with parameters anticipated for *in vivo* rat experiments (figure 11) were conducted for 160 μm diameter electrodes. Unannealed

array data was omitted because devices must be thermoformed prior to implantation in order to obtain the appropriate three-dimensional structure. Note that the voltage transients of PtIr coated devices remain well

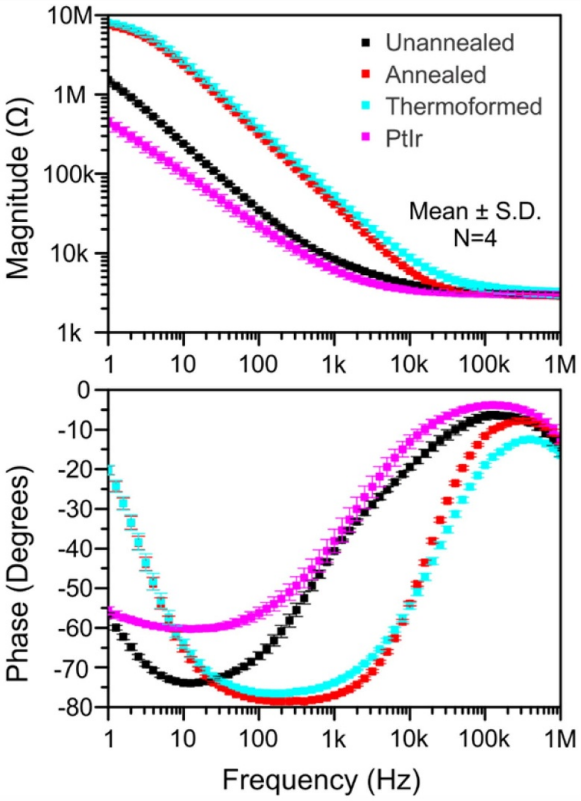

Figure 9. Electrochemical impedance magnitude (a) and phase (b) at different stages of device processing (1 × PBS, 25 °C).

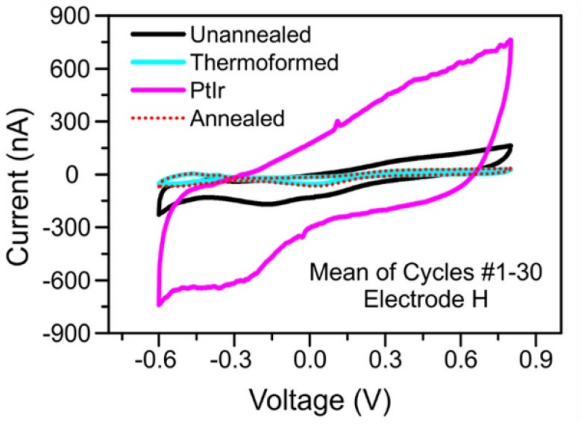

Figure 10. Cyclic voltammetry at different stages of device processing. PtIr devices exhibited the widest plots (1 × PBS, 25 °C).

within the water window [43] compared to uncoated devices.

4.3. Animal testing

Several surgeries were performed in an iterative manner on enucleated eyes as well as in whole animal in order

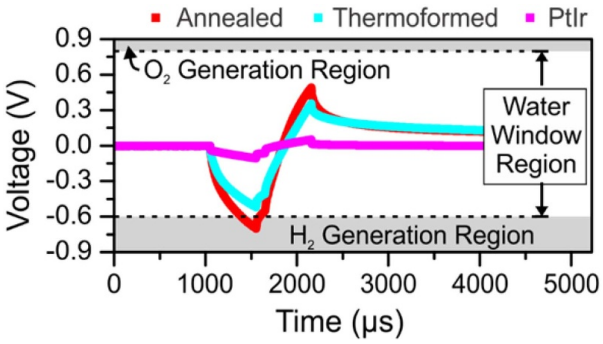

Figure 11. Pulse test results at different stages of device processing. PtIr reduced voltage transients compared to bare Pt (1 × PBS, 25 °C).

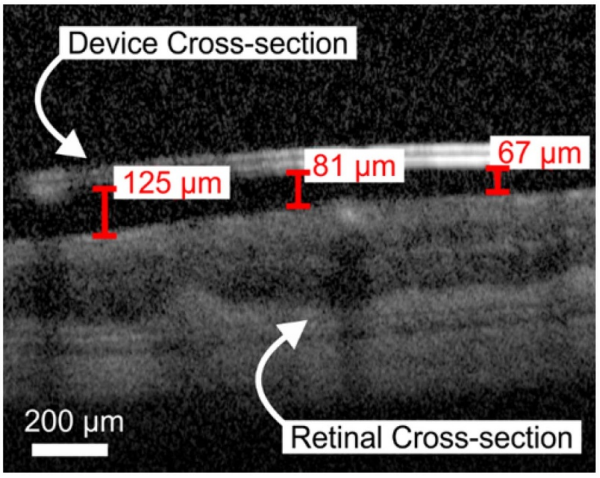

Figure 12. Optical coherence tomography image of sham array tip cross-section and retina (4 weeks post-surgery).

to understand the interaction between the rat anatomy and Parylene device. OCT images (figure 12) illustrate that the array geometry closely matched retinal curvature. This experiment was designed with a target duration of 4 weeks. Since the implant was well-tolerated without inflammation or significant shifts in location well past the target duration, the experiment was terminated at week 6.

Afterwards, complete MEAs were implanted in an acute trial (<5 h). Figure 13(a) illustrates the proptosing of an eye using a silk suture hooked under the eyelid in order to provide access to scleral tissue. In figure 13(b), the array was inserted and sutured into the ocular orbit. No notable friction against ocular tissue and device was reported during the insertion.

Figure 13(c) shows the connection scheme between the implanted device and a potentiostat system which applied EIS to assess electrode viability. The contact pad region of the device was potted in marine epoxy and a flat flexible cable was fed into a breakout board. Immediately prior to implantation, EIS was conducted in 1 × PBS and three out of eight electrodes on this retinal array

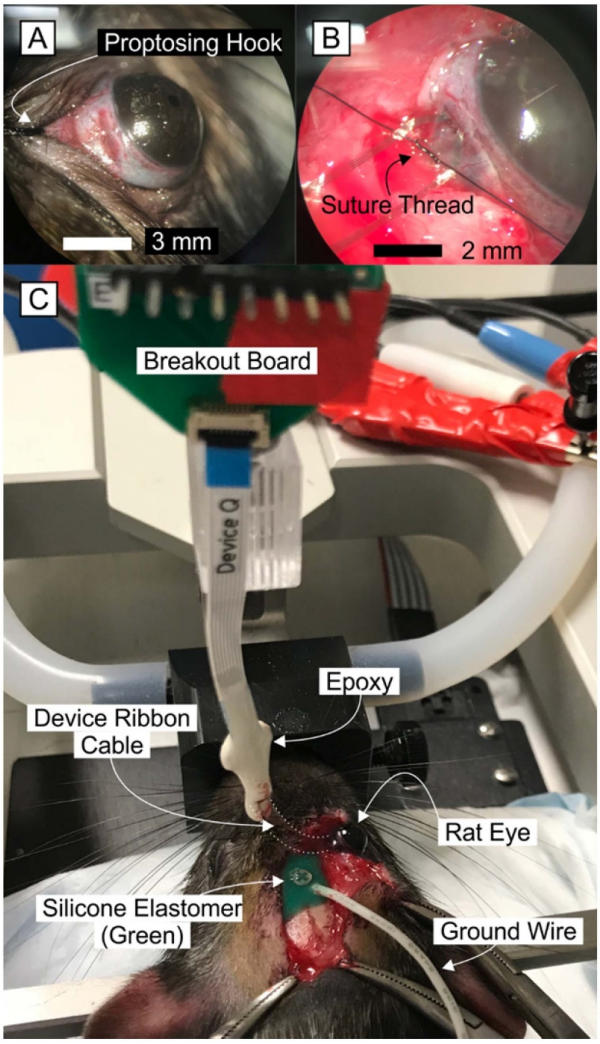

Figure 13. (a) The eye was proptosed to enable more access to the sclera then (b) the retinal array was sutured on. (c) Connection scheme from implanted array to potentiostat.

were deemed functional—meaning that their electrochemical spectra resembled those of benchtop data. Nonfunctional electrodes displayed MΩ or GΩ impedance magnitudes and approximately −90° impedance phase at higher frequencies (figure S4). This is indicative of an open circuit that may have resulted from wire breakage by damage from shipping, packaging, mishandling, or thermoforming complications.

EIS measurements after surgery while the array was inside the orbit revealed that the three previously functional electrodes remained functional (figure S4). Minor differences in spectra are attributed to the different electrolyte (1 × PBS vs. vitreous humor). This indicated that no significant device damage was sustained from the implantation procedure and illustrated the robustness of the device against potential surgical trauma.

5. Discussion

Failure modes due to difficulties in device fixation to the orbit were one of the largest anticipated challenges. However, fixation was successfully achieved despite being unable to use retinal tacks. After completing practice trials, suturing the device with surgical nylon thread through aforementioned suture holes consistently resulted in minimal inflammation and suitable fixation of the array post-operation (fundus imaging showed negligible translation with respect to optic nerve over time). It is noteworthy that proptosing the orbit is critical to ensure comfortable access to the pars plana and that only the two suture holes nearest to the electrodes should be used due to the limited availability of scleral surface area. The rat's tolerance to the implantable device is most likely attributable to Parylene C's biocompatibility as well as the gentle curvature of the thermoformed region which exhibits spring-like behavior if contact is briefly made with the retina during saccadic eye movement

However, obtaining thermoformed devices with a high yield of functional electrodes remained challenging. Matching the retinal curvature (r ≈ 2.5 mm) was relatively simple to accomplish but administering the second bend which routes the ribbon cable back towards the headcap (r ≈ 200 μm) was nontrivial. This second bend radius was selected to be as close as possible to the thickness of the rat sclera [44] while following guidelines established through bend tests of similar Parylene-Pt-Parylene sandwich devices [45]. Unfortunately, microscopic cracks could be observed in the Pt wires at the second bend region, rendering about 48% of electrodes nonfunctional due to the unintended open circuit. Nevertheless, batch fabrication with high electrode yield immediately prior to thermoforming enabled production of arrays suitable for preliminary *in vivo* experiments. Slightly relaxing the severity of the second bend (r ≈ 400 μm) is recommended to improve electrode yield as well as scleral fit because closer surgical observation revealed that conjunctival fatty tissue contributed to previously unaccounted for additional scleral thickness.

The tight second bend is required for the design presented in order to meet the anatomical requirements of the rat eye and the desired close fit to the retina. This report presents one possible geometry to address these specifications and new, alternative geometries are also being explored that do not require the second bend.

Although the first bend consistently yielded functional electrodes that matched the rat retinal curvature on average, limitations exist which preclude a perfectly flush geometry. Unlike the cylindrical dowel pins of the thermoforming mold, the rat ocular cross-section is not a perfect circle and instead is slightly oblong [27]. The manual process of surgical attachment also introduces alignment variability. However, because the epiretinal approach provides direct access to retinal ganglion cells, electrodes placed up to 1000 μm away from the retina have been reported by others to elicit electrically evoked responses in the visual cortex [20]. In this work, sutures provide mechanical fixation at the second bend region which caused electrodes closer to the array tip to be slightly farther away from the retina. For this reason, one set of electrodes

features larger diameters along lower latitudes of the ocular orbit whereas the other is constant to investigate electrical field attenuation dynamics in future *in vivo* work.

Although higher electrode count would be preferred, the need for larger electrode diameters for stimulation and rat anatomical constraints resulted in a maximum of eight electrodes. For reference, the Argus II device features 60 electrodes with the goal of providing enough spatial resolution to partially restore sight to human patients. Because this work aims to enable and accelerate retino-visual research in rats by generally eliciting electrically evoked responses in the brain, eight electrodes are presumed to be more than sufficient when compared against previous single needle electrode configurations.

Electrochemical data presented earlier suggested that PtIr coating improved charge storage capacity which may increase the likelihood of generating electrically evoked responses. This was evidenced by reduced impedance magnitude at 1 kHz in EIS and a generally wider CV plot. However, the same appears to be true for unannealed devices when compared against annealed and thermoformed devices. This potentially misleading electrochemical difference is due to different rates of undesired yet finite water and ion permeability into the Parylene polymer.

Thermal treatment will induce molecular rearrangement of semicrystalline and amorphous regions of Parylene which increases crystallinity and reduces liquid permeability [46]. Therefore, unannealed devices experience greater fluid penetration into the Parylene and thus larger rates of unwanted electrochemical reactions occur between the metal at the wires and the electrode backside. More current flow may occur for a given voltage perturbation signal amplitude in potentiostatic EIS. Because the impedance magnitude represents the ratio between the supplied voltage and measured current amplitudes, unannealed devices exhibit lower impedance magnitudes at lower frequency regimes where electrode–electrolyte interface dynamics dominate (<10 kHz) [47].

Similarly, wider CV plots for unannealed devices are a consequence of undesired excess electrochemical current from unwanted water and ion permeation. Furthermore, hydrogen adsorption/desorption and Pt-oxide redox reactions clearly produce characteristic peaks and valleys in the CV plots of thermally treated devices. This suggests that electrochemical reactions are successfully confined to the Pt-electrolyte interface for thermally treated devices, but such electrochemical signatures are blurred in the unannealed case due to leaky dielectric contribution from soaked Parylene. These results highlight that thermoforming is well-suited for the dual purpose of improved electric insulation as well as geometric modification to match anatomical constraints.

Lastly, preliminary implantations demonstrated surgical feasibility of the rat epiretinal array device. This represents a critical first step towards realizing an entire epiretinal system. Additional animal operations will be required in order to gain insight on other systemic complexities such as packaging, communication via the wireless headstage, and integration with visual cortex recording. Such components may be purchased from commercial vendors, whereas the epiretinal rat array necessitated customized research and design which was accomplished through this work.

6. Conclusion

An implantable epiretinal stimulation array for rats was designed, fabricated, and tested in order to serve as a tool to accelerate research on vision and neuroscience. This work articulated nuances in surgical challenges associated with the rat retinal model which soft polymer neural interfaces are uniquely positioned to overcome.

Anatomically imposed geometric constraints of the rat retina were addressed via three-dimensional thermoforming of Parylene and iterative lessons learned through surgical trials. Benchtop electrochemical tests of the device revealed superior electrical insulation due to thermal treatment of the Parylene and that PtIr electroplating demonstrated improved charge storage capacity. *In vivo* tests demonstrated chronic biocompatibility for up to 6 weeks with non-metallized sham devices. Functional devices containing electrodes displayed electrical integrity post-surgery. Future studies will investigate amenability to chronic epiretinal stimulation *in vivo* and integration with other systemic components.

Acknowledgments

This work was funded by the NSF under award number CBET-1343193. The authors would also like to thank Dr. Donghai Zhu and Alfonso Jimenez of the Keck Photonics Laboratory for microfabrication assistance, Dr. Juan Carlos Martinez for performing the preliminary sham surgeries, and Gregory Weiland of Platinum Group Coatings LLC for providing PtIr coatings. The authors would also like to acknowledge the members of the Biomedical Microsystems Laboratory at the University of Southern California for their insightful thoughts and discussion in the preparation of this work. Authors CDL, AP, and JDW have a financial interest in the commercialization of electrodeposited platinum-iridium.

ORCID iDs

E Yoon https://orcid.org/0000-0002-5010-0451
J Wong https://orcid.org/0000-0001-5329-8638
S Elyahoodayan https://orcid.org/0000-0003-3684-2018
E Meng https://orcid.org/0000-0003-0981-9197

References

[1] Wu W, Peters W H and Hammer M E 1987 Basic mechanical properties of retina in simple elongation *J. Biomech. Eng.* **109** 65–7
[2] Stronks H C and Dagnelie G 2014 The functional performance of the Argus II retinal prosthesis *Expert Rev. Med. Devices* **11** 23–30
[3] Weiland J D and Humayun M S 2014 Retinal Prosthesis *IEEE Trans. Biomed. Eng.* **61** 1412–24

[4] Niketeghad S and Pouratian N 2019 Brain machine interfaces for vision restoration: the current state of cortical visual prosthetics *Neurotherapeutics* **16** 134–43

[5] Moritz C T 2018 Now is the critical time for engineered neuroplasticity *Neurotherapeutics* **15** 628–34

[6] Rosa A M, Silva M F, Ferreira S, Murta J and Castelo-Branco M 2013 Plasticity in the human visual cortex: an ophthalmology-based perspective *Biomed. Res. Int.* **2013** 568354

[7] Damle S, Y H L and Freeman W R 2017 High visual acuity retinal prosthesis: understanding limitations and advancements toward functional prosthetic vision *Retina* **37** 1423–7

[8] Meyer J 2002 Retina implant—a bioMEMS challenge *Sensors Actuators* A **97** 1–9

[9] Hesse L, Schanze T, Wilms M and Eger M 2000 Implantation of retina stimulation electrodes and recording of electrical stimulation responses in the visual cortex of the cat *Graefe's Arch. Clin. Exp. Ophthalmol.* **238** 840–5

[10] Gerding H, Benner F P and Taneri S 2007 Experimental implantation of epiretinal retina implants (EPI-RET) with an IOL-type receiver unit *J. Neural Eng.* **4** S38

[11] Güven D *et al* 2005 Long-term stimulation by active epiretinal implants in normal and RCD1 dogs *J. Neural Eng.* **2** S65

[12] Koh A E *et al* 2019 Retinal degeneration rat model: A study on the structural and functional changes in the retina following injection of sodium iodate *J. Photochem. Photobiol. B Biol.* **196** 111514

[13] Fletcher E L, Jobling A I, Vessey K A, Luu C, Guymer R H and Baird P N 2011 Animal models of retinal disease *Prog. Mol. Biol. Transl. Sci.* **100** 211–86

[14] Bertschinger D R *et al* 2008 A review of in vivo animal studies in retinal prosthesis research *Graefe's Arch. Clin. Exp. Ophthalmol.* **246** 1505–17

[15] Mathieson K *et al* 2012 Photovoltaic retinal prosthesis with high pixel density *Nat. Photon.* **6** 391–7

[16] Kansara V, Muya L, Wan C and Ciulla T A 2020 Suprachoroidal delivery of viral and nonviral gene therapy for retinal diseases *J. Ocul. Pharmacol. Ther.* **00** 1–9

[17] Pardue M T, Phillips M J, Yin H, Fernandes A, Cheng Y, Chow A Y and Ball S L 2005 Possible sources of neuroprotection following subretinal silicon chip implantation in RCS rats *J. Neural Eng.* **2** S39

[18] Goetz G A and Palanker D V 2016 Electronic approaches to restoration of sight *Rep. Prog. Phys.* **79** 096701

[19] Gabel V P 2017 *Artificial Vision* vol 1 (Berlin: Springer)

[20] Balthasar C *et al* 2008 Factors affecting perceptual thresholds in epiretinal prostheses *Investig. Ophthalmol. Vis. Sci.* **49** 2303–14

[21] Chuang A T, Margo C E and Greenberg P B 2014 Retinal implants : a systematic review *Br. J. Ophthalmol.* **98** 852–6

[22] Nimmagadda K and Weiland J D 2018 Retinotopic responses in the visual cortex elicited by epiretinal electrical stimulation in normal and retinal degenerate *Rats Trans. Vis. Sci. Tech.* **7** 33

[23] Chan L L H, Lee E J, Humayun M S and Weiland J D 2011 Both electrical stimulation thresholds and SMI-32-immunoreactive retinal ganglion cell density correlate with age in S334ter line 3 rat retina *J. Neurophysiol.* **105** 2687–97

[24] Ortigoza-Diaz J, Scholten K, Larson C, Cobo A, Hudson T, Yoo J, Baldwin A, Weltman Hirschberg A and Meng E 2018 Techniques and considerations in the microfabrication of parylene c microelectromechanical systems *Micromachines* **9** 422

[25] Petrossians A, Whalen J J, Weiland J D and Mansfeld F 2011 Electrodeposition and characterization of thin-film platinum-iridium alloys for biological interfaces *J. Electrochem. Soc.* **158** S15

[26] Cogan S F, Troyk P R, Ehrlich J and Plante T D 2005 In vitro comparison of the charge-injection limits of activated iridium oxide (AIROF) and platinum-iridium microelectrodes *IEEE Trans. Biomed. Eng.* **52** 1612–4

[27] Lozano D C and Twa M D 2013 Development of a rat schematic eye from in vivo biometry and the correction of lateral magnification in SD-OCT imaging *Investig. Ophthalmol. Vis. Sci.* **54** 6446–55

[28] Juan E, Hickingbotham D and Machemer R 1985 Retinal tacks *Am. J. Ophthalmol.* **99** 272–4

[29] Gregori N Z, Davis J L and Rizzo S 2016 Bimanual technique for retinal tacking of epiretinal prosthesis *Retina* **36** 199–202

[30] Wallace D J, Greenberg D S, Sawinski J, Rulla S, Notaro G and Kerr J N D 2013 Rats maintain an overhead binocular field at the expense of constant fusion *Nature* **498** 65–69

[31] Shah S, Hines A, Zhou D, Greenberg R J, Humayun M S and Weiland J D 2007 Electrical properties of retinal—electrode interface *J. Neural Eng.* **4** S24

[32] Ahuja A K, Behrend M R, Whalen J J, Humayun M S and Weiland J D 2008 The dependence of spectral impedance on disc microelectrode radius *IEEE Trans. Biomed. Eng.* **55** 1457–60

[33] Sui X, Huang Y, Feng F, Huang C, Chan L L H and Wang G 2015 3D finite element modeling of epiretinal stimulation: impact of prosthetic electrode size and distance from the retina *Int. J. Artif. Organs* **38** 277–87

[34] Kim B J, Chen B, Gupta M and Meng E 2014 Formation of three-dimensional Parylene C structures via thermoforming *J. Micromech. Microeng.* **24** 065003

[35] Ray A *et al* 2011 Impedance as a method to sense proximity at the electrode-retina interface *IEEE Trans. Neural Syst. Rehabil. Eng.* **19** 696–9

[36] Salinas-Navarro M, Mayor-Torroglosa S, Jiménez-López M, Avilés-Trigueros M, Holmes T M, Lund R D, Villegas-Pérez M P and Vidal-Sanz M 2009 A computerized analysis of the entire retinal ganglion cell population and its spatial distribution in adult rats *Vision Res.* **49** 115–26

[37] Thomasy S M, Eaton J S, Timberlake M J, Miller P E, Matsumoto S and Murphy C J 2016 Species differences in the geometry of the anterior segment differentially affect anterior chamber cell scoring systems in laboratory animals *J. Ocul. Pharmacol. Ther.* **32** 28–37

[38] Lee C D, Hudak E M, Whalen J J, Petrossians A and Weiland J D 2018 Low-impedance, high surface area Pt-Ir electrodeposited on cochlear implant electrodes *J. Electrochem. Soc.* **165** G3015

[39] Gutierrez C A, Lee C D, Kim B J and Meng E 2011 Epoxy-less packaging methods for electrical contact to Parylene-based flat flexible cables *The 16th Int. Conf. on Solid-State Sensors, Actuators and Microsystems (TRANSDUCERS & EUROSENSORS XXVI)* pp 2299–302

[40] Silue T A, Mannikanti S and Peixoto N 2017 Electrochemical characterization of vitreous humor *Procedia Technol.* **27** 301–3

[41] Hudak E M *et al* 2017 Electron transfer processes occurring on platinum neural stimulating electrodes: calculated charge-storage capacities are inaccessible during applied stimulation *J. Neural Eng.* **14** 1–24

[42] Lee W R *et al* 2017 A convex-shaped, PDMS-parylene hybrid multichannel ECoG-electrode array *Proc. Annu. Int. Conf. IEEE Eng. Med. Biol. Soc. EMBS* **2017** 1093–6

[43] Cogan S F, Hara S and Ludwig K A 2018 *The Safe Delivery of Electrical Currents and Neuromodulation* vol 2 (Amsterdam: Elsevier) (https://doi.org/10.1016/B978-0-12-805353-9.00007-3)

[44] Burgess A *et al* 2016 Rat optic nerve head anatomy within 3d histomorphometric reconstructions of normal control eyes *Exp. Eye Res.* **15** 477–91

[45] Lee C D and Meng E 2015 Mechanical properties of thin-film parylene–metal–parylene devices *Front. Mech. Eng.* **1** 1–14
[46] Jackson N, Stam F, O'Brien J, Kailas L, Mathewson A and O'Murchu C 2016 Crystallinity and mechanical effects from annealing Parylene thin films *Thin Solid Films* **603** 371–6
[47] Little C A E, Orloff N D, Hanemann I E, Long C J, Bright V M and Booth J C 2017 Modeling electrical double-layer effects for microfluidic impedance spectroscopy from 100 kHz to 110 GHz *Lab Chip* **17** 2674–8